

# 1 A search for highly ionizing, short tracks at the CMS detector

In this chapter a search for highly ionizing, short tracks is presented. The chapter will be structured as follows: In Sec. 1.1 a motivation will be given, followed by an overview of the general search strategy in Sec. 1.2. As the variable  $dE/dx$  plays a crucial role in this analysis, a general introduction and different possible parametrizations will be introduced in Sec. 1.3. In this context also the conducted offline calibration of the silicon pixel detector will be explained. After presenting the simulated SM and signal samples which were used in this analysis (Sec. 1.4) the event selection is shown (Sec. 1.5). Then, the various sources of background are characterized (Sec. 1.6) and the methods to estimate their size are presented (1.7). As a final step an optimization in the search sensitivity was done, which can be found in Sec. 1.8. The chapter concludes by presenting the results of this analysis in Sec. 1.10, and after a short introduction to the statistical methods of limit setting (Sec. 1.9), the results will be interpreted in the context of Supersymmetry (Sec. 1.11).

## 1.1 Motivation

As it was already pointed out in Chap. ??, Supersymmetry is able to offer solutions to unexplained phenomena in astrophysics and can solve the shortcomings of the Standard Model of particle physics. Unfortunately, due to the unknown mechanism of supersymmetry breaking, the most general parametrization of Supersymmetry introduces over 100 new dimensions which opens up an incredibly huge phenomenologically rich space, leading to very different possible signature at particle colliders. During the Phase I run at the LHC in 2012, a variety of different searches, optimized on the hunt for supersymmetry were conducted. At the CMS and at the ATLAS experiments, taking data from proton-proton collisions, a strong focus was put on the search for hints of SUSY in the strong production sector (e.g. [1–3]). This led already to a wide exclusion in SUSY space, which nevertheless still offers some very interesting non-excluded parameter regions. The search for SUSY in more "exotic" regions gains therefore more and more attention. Typical SUSY scenarios which are not easily excluded by the general SUSY searches consists of so-called compressed spectra, where two or more particles are nearly degenerate in their masses. When mother and daughter particles are almost mass-degenerate, the remaining decay product in a two body decay can be very soft in  $p_T$ , making those scenarios very challenging to search for. Thus supersymmetric scenarios with compressed spectra are usually much weaker constrained.

One especially interesting scenario in R-parity conserved Supersymmetry is where the lightest neutralino ( $\chi_1^0$ ) is almost mass-degenerate with the lightest chargino ( $\chi_1^\pm$ ). Such a mass-degeneracy naturally occurs in case of a wino-like neutralino and chargino, as the mass gap is fully determined by higher loop correction as explained in Sec. ?. Models containing a wino-like neutralino can especially be interesting in explaining the sources

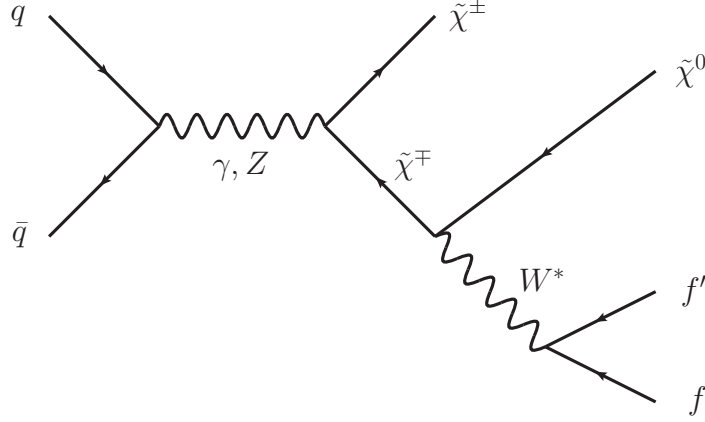


Figure 1.1: Feynman diagram showing a possible production mechanism of a chargino pair and the decay channel of a chargino.

of the relic density. Although such a model is not able to make up the full relic density thermally produced for  $m_{\chi_1^0} \lesssim 2.9$  TeV from the lightest neutralino [4], it can still be the dominant part when it is non-thermally produced via the decay of a long-lived particle [5], which is the chargino in this scenario and gains its long-lifetime due to the phase-space suppression because of the mass degeneracy with the neutralino (see Sec. ??). Additionally, due to the large annihilation cross-sections for a wino-like neutralino [6], these models would result in strong signals in indirect searches.

A chargino can be produced via chargino pair production through a photon or a Z boson exchange. The chargino decays then via a virtual W boson to the lightest neutralino and fermion-fermion pair (e.g. a pion). This process is illustrated in the Feynman diagram shown in fig. 1.1.

Other possible production channels are the exchange of a supersymmetric Higgs boson or via a t-channel squark exchange. The corresponding Feynman diagrams for the tree level production channels are shown in Fig. 1.2.

Another possibility of chargino production is the chargino neutralino production channel. On tree level, there exist two production mechanisms: the s-channel W boson exchange and the t-channel squark exchange, see Fig. 1.3 for the Feynman diagrams.

Even if the presented supersymmetric model where  $\chi_1^\pm$  and  $\chi_1^0$  are nearly mass-degenerate leads to more exotic signatures at the CMS experiment, there have been already several analyses conducted in CMS which are in principle (even not all were designed to be) sensitive to these models. Among those are a search for long-lived charged particles [7], which was mainly designed for particles which have such a long lifetime that they travel through the full detector without decaying and a search for disappearing tracks [8] which looked for rather intermediate lifetimes, where the charginos decay already inside the tracker. Within [8], a study was done, based on an interpretation exercise [9] within the phenomenological MSSM (see Sec. ?? for a detailed introduction to the pMSSM), which

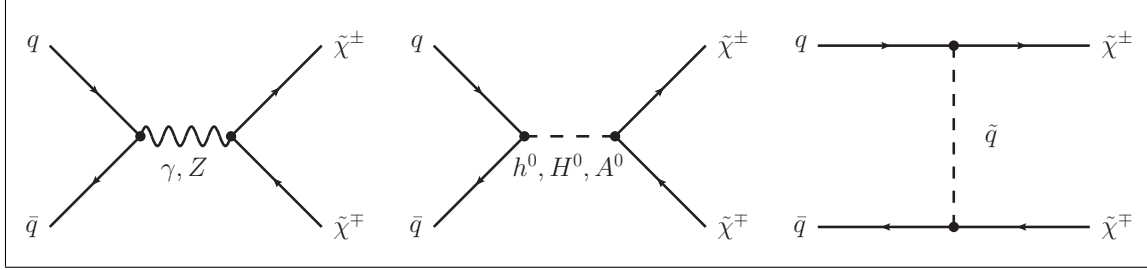


Figure 1.2: Main tree level diagrams for chargino pair production.

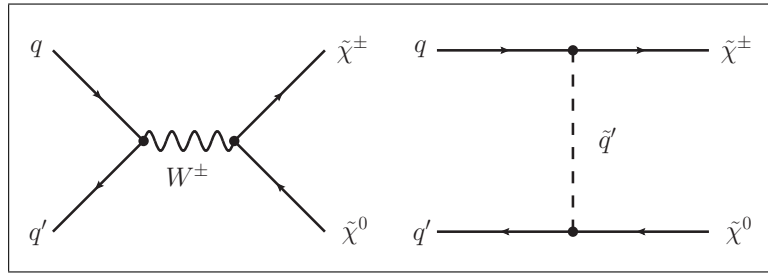


Figure 1.3: Main tree level diagrams for chargino neutralino production.

tests the exclusion power of various analyses done at CMS.

In Fig. 1.4, the exclusion power of the search for long-live charged particles [7] in red, the search for disappearing tracks [8] in purple and a collection of various SUSY analysis from [10] in blue over the chargino mass is shown. In black the distribution of the unexcluded pMSSM parameter points vs. the chargino lifetime can be seen. The sampling of the parameter space points was done according to a pre-CMS likelihood function, which takes into account electroweak precision measurements, etc. In the lower part of Fig 1.4, the excluded fraction of pMSSM points is shown. It can be seen, that the more general SUSY searches are mostly sensitive to shorter chargino lifetimes ( $c\tau \lesssim 10$  cm)<sup>1</sup>, whereas the search for long-lived particles shows very good sensitivity for lifetimes  $> 100$  cm. The search for disappearing tracks is sensitive on supersymmetric models with chargino lifetimes between  $35 \text{ cm} \lesssim c\tau \lesssim 100 \text{ cm}$ .

This analysis is targeting the gap between the disappearing track search (purple area) and the searches which are sensitive to instantaneously decaying charginos (blue area). The idea is to make use of the variable  $dE/dx$  which can be very discriminating for particles with high mass. The challenges of such a search and the general strategy of this analysis will be presented in the next section.

## 1.2 General search strategy

When searching for supersymmetric models with long-lived  $\tilde{\chi}_1^\pm$ , the strategy is of course highly dependent on the actual lifetime of the chargino. For long lifetimes, the chargino

<sup>1</sup>It should be mention, that because the impossibility of simulating long-lived charginos in from the generator, it could not be tested to which exact upper lifetime, the searches are sensitive. But it is reasonable to argue, that they won't be sensitive to longer lifetimes, as these are usually high background searches

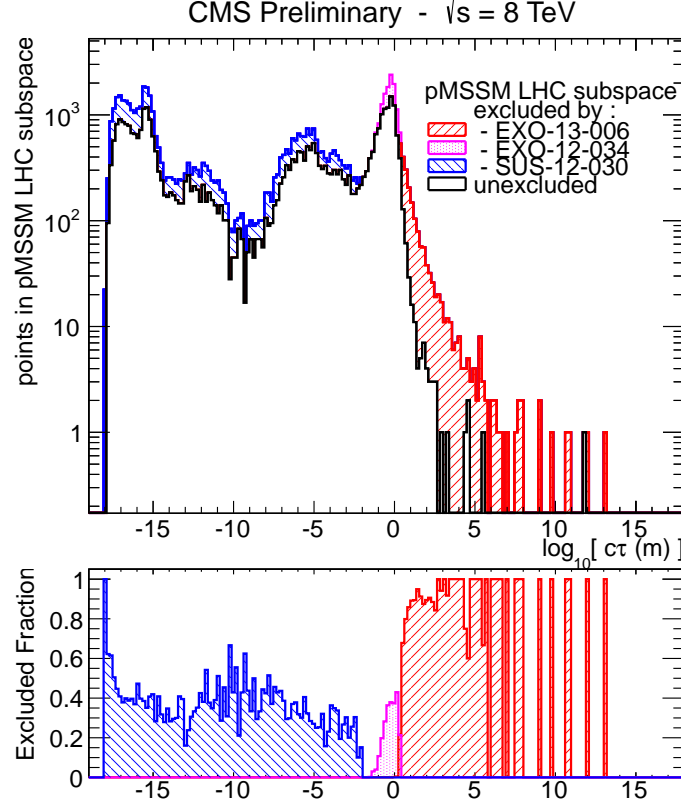


Figure 1.4: Exclusion power of various analyses dependent on chargino lifetime  $[c\tau]$ . Lower part of the plot shows the excluded fraction. Taken from: [click here](#).

can reach the muon chambers and can be reconstructed as a muon (even with a longer time-of-flight). For lower lifetimes, the chargino can already decay inside the detector (e.g. the tracker), thus not leading to a reconstructed muon in the event, but only to an isolated track in the tracker. The detector signatures of these two scenarios are visualised in Fig 1.5, where in a cross-sectional view of the CMS detector simulated chargino-chargino events are shown. As mentioned before, this analysis targets a search for supersymmetry with charginos of lifetimes between  $10 \text{ cm} \lesssim c\tau \lesssim 40 \text{ cm}$ . That means that the charginos decay rather early in the detector, even at the beginning of the tracker. The distinct challenges of such an analysis, shall be listed in the following passage.

First of all, in case R-parity (see Sec. ??) is conserved, one of the decay products of the chargino, which is the lightest neutralino  $\tilde{\chi}_1^0$  is stable, thus travelling through the whole detector only weakly interacting. Therefore it is not detectable. The other chargino decay product, e.g. a pion, can be hardly reconstructed, mainly because it does not originate from the primary vertex (if the chargino reaches the detector before its decay), but secondarily because it is very low in momentum because of the mass-degeneracy between  $\tilde{\chi}_1^\pm$  and  $\tilde{\chi}_1^0$ . The momentum of the decay product is of course highly dependent on the actual mass gap between the neutralino and the chargino. The typical momentum of a pion originating

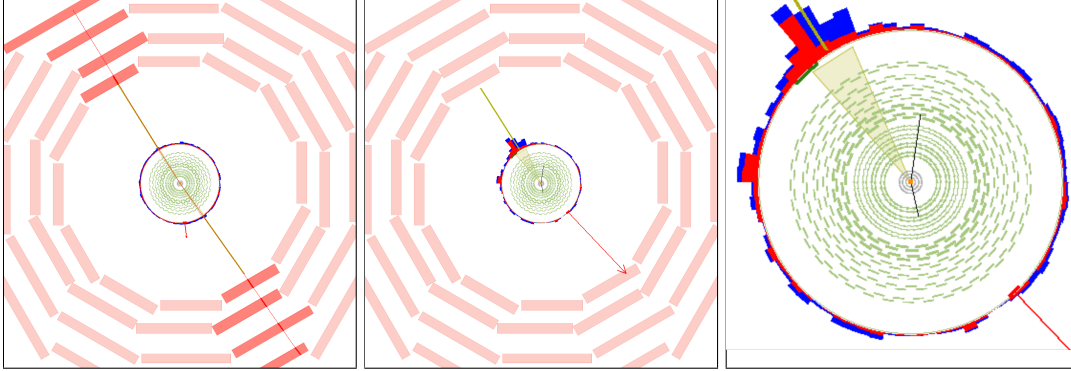


Figure 1.5: Visualisation of possible signatures of a chargino pair produced with a lifetime of  $c\tau = 10$  m (left) and a lifetime of  $c\tau = 0.5$  m (middle and right). In the left picture, both charginos are reconstructed as muons, which can be seen in the energy deposition in the muon chambers (red boxes). In the middle picture both charginos are only visible as tracks in the tracker (black lines), where both trajectories end inside the silicon tracker, showing the decay point of the corresponding chargino. The right picture is a zoom of the picture in the middle. Here only the cross-section of the tracker (green wavy lines) is displayed. The red arrow shows the missing transverse energy in the event.

from a chargino to neutralino decay is in the  $\tilde{\chi}_1^\pm$  rest frame of the order

$$p_\pi \sim \sqrt{m_{\tilde{\chi}_1^\pm} - m_{\tilde{\chi}_1^0} - m_\pi}.$$

A  $p_T$  distribution of the pion for a simulation with  $\sqrt{s} = 8$  TeV can be found in Fig. 1.7 for a mass gap between  $\tilde{\chi}_1^\pm$  and  $\tilde{\chi}_1^0$  of  $\Delta m = 150$  MeV. The  $p_T$  distribution peaks at  $\sim 100$  MeV and ends at  $p_T \sim 400$  MeV. When the transverse momentum of a particle is very low, the particle trajectory is much more bended compared to a particle with higher  $p_T$  (see Fig. 1.7 for illustration), thus making the detection of such a particle very challenging. Because of the stronger bending, the track reconstruction efficiency decreases for particles with a transverse momentum below 1 GeV rapidly, ending at around 40% for isolated pions with a  $p_T$  of 100 MeV (see [11]).

Taking the hard or even impossible detection of the decay products of the chargino, this lead to the fact, that besides the (short) track of the chargino, nothing can be seen in the detector. Unfortunately, there is no dedicated track trigger at CMS, which makes a specific detection of those events with the help of the chargino track impossible. To be able to search for these models, one therefore needs to take advantage of higher order contributions to the feynman diagrams shown in the previous sections (Figs. 1.2,1.3), resulting in initial state radiation (ISR). When the initial quarks radiate a high  $p_T$  gluon, the resulting jet can be detected and can offer a possibility to search for isolated tracks in the tracker. The non-detection of the chargino's decay products plus a high  $p_T$  ISR jet lead additionally to missing transverse energy (MET) in the event. Exploiting these two circumstances, it is possible to detect chargino-pair or chargino-neutralino events with the help of Jet+MET triggers.

To select possible charginos in an event, additional requirements for isolated, high  $p_T$

tracks are needed. Those tracks can be eventually disappearing, which means that the track does not cross the full pixel and strip detector. This can happen, when the chargino decays inside the tracker. For very low lifetimes, the tracks can be very short and can have only a few hits in the detector. To define a helical path five parameters are needed, therefore a minimum of three hits are required to be able to reconstruct a particle's trajectory (see [11]). In this analysis, the massiveness of the charginos shall be exploited, on the one hand by selecting only high  $p_T$  tracks, but on the other hand by requiring a high energy deposition per path length ( $dE/dx$ ). The energy deposition depends quadratically

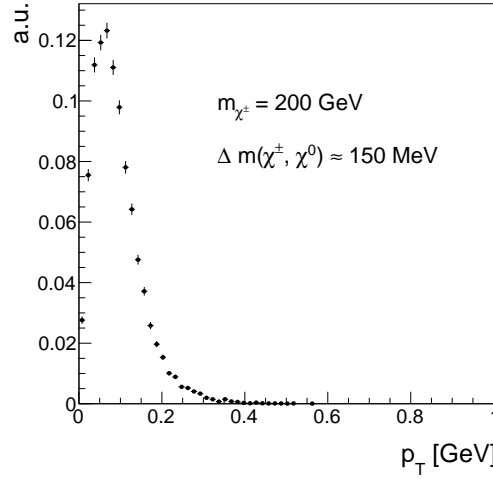


Figure 1.6: Transverse momentum distribution of pions coming from chargino decay into a neutralino with a mass gap of 150 MeV.

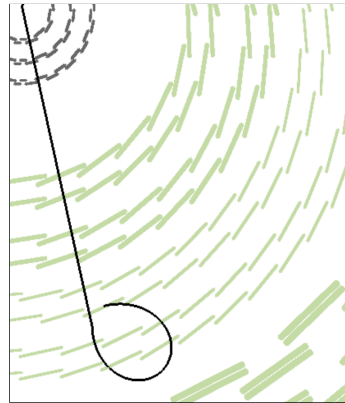


Figure 1.7: Cross-sectional view of the tracker (different tracker layers are illustrated with wavy green lines) and a simulated chargino track (black line) decays to a pion (bended black line).

on the particle's mass for low velocities ( $0.2 < \beta\gamma < 0.9$ ).

$$\langle \frac{dE}{dx} \rangle = K \frac{m^2}{p^2} + C$$

thus constitute a very nice discriminating variable for massive particles against SM particles.

A specific challenge for this analysis is hence the combination of searching for short tracks and utilising the measurement of the energy deposition of the chargino. For a short track, eventually only passing the first couple layers of the whole tracker system, the pixel tracker becomes obviously very important. This means that a good energy measurement in the pixel system is of great importance to this analysis. However, no other CMS analysis used the energy information of the pixel tracker so far. That means, that a thoroughly study of the quality of the pixel energy calibration needs to be undertaken, and in case the energy calibration is not sufficient, a further energy calibration needs to be carried out.

### 1.2.1 Comparison to existing searches

As already mentioned before, there are several analyses at CMS at  $\sqrt{s} = 8$  TeV with  $20 \text{ fb}^{-1}$  data, which are sensitive to intermediate lifetime charginos. Most notably, the search for long lived-charged particles [7] and the search for disappearing tracks [8]. An improvement in sensitivity to shorter lifetimes compared to these analysis shall be achieved in a twofold way: First, the selection in this analysis shall also include very short tracks. And secondly, also the inclusion of the variable  $dE/dx$  as discriminating variable shall increase the search sensitivity compared to [8].

In [7], for every track a minimum number of eight hits, whereas in [8] a minimum of seven hits were required. This can be very inefficient for shorter lifetimes, where most of the charginos decay already shortly after the pixel tracker. In Fig. 1.8, the normalized distribution of the number of measurements ( $N_{\text{hits}}$ ) is shown. It can be seen, that for lower lifetimes,  $N_{\text{hits}}$  is peaking at the minimal possible value which is needed for track reconstruction of  $N_{\text{hits}} = 3$ . For higher lifetimes the distribution shifts to higher values with a second peak at  $N_{\text{hits}} \sim 17$ . However, a notably fraction of  $\sim 40\%$  of tracks has still a number of measurements below  $N_{\text{hits}} < 8$ .

Additionally, the search for disappearing tracks (which targets models with charginos decaying inside the tracker) did not make use of the high energy deposition of heavy particles. Although this variable was indeed used in the search for long-lived particles, this search was not especially designed for intermediate lifetimes (e.g. no muon veto on the selected tracks was required), thus it shows less sensitivity compared to the disappearing track search in the lifetime region between  $35 \text{ cm} \lesssim c\tau \lesssim 100 \text{ cm}$  (see Fig 1.4).

Therefore, the general search strategy of the presented analysis is to unite the strategies of [7] and [8] and to lower the strong selection on the number of hits in these analyses to get an optimized selection for lifetimes around  $10 \text{ cm} \lesssim c\tau \lesssim 40 \text{ cm}$ .

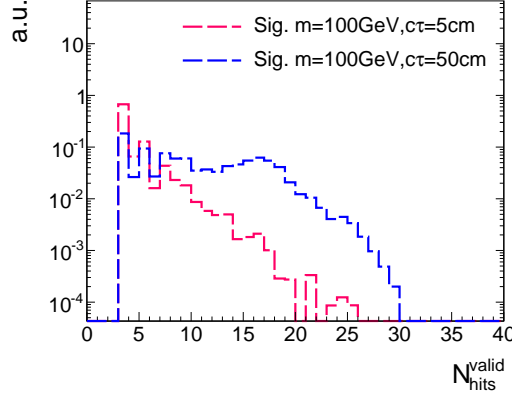


Figure 1.8: Number of measurements in the tracker system  $N_{\text{hits}}$  for two different signal lifetimes ( $c\tau = 5$  cm and  $c\tau = 50$  cm). The lower lifetime is much more rapidly falling and peaking at the lowest number of possible measurements of three. For a lifetime of  $c\tau = 50$  cm, a second peak at  $\sim 17$  hits appears corresponding to the number of measurements when crossing all pixel barrel (3) and strip inner and outer barrel (6 from stereo and 8 from normal) layers. More information on the generation of the simulated signal samples can be found in Sec. ??

### 1.3 Improved $dE/dx$ measurement of short tracks

It was already pointed out, that the inclusion of the pixel energy measurements can increase the sensitivity when searching for short tracks. While the silicon strip detector has already been calibrated as part of the search for long-lived charged particles [7], there was never an offline calibration done for the pixel silicon tracker. To increase the discrimination power of  $dE/dx$ , such a calibration procedure was therefore conducted within this PHD thesis.

#### 1.3.1 Measuring $dE/dx$

The mean energy loss per path length of particles travelling through a layer of material can be described with the Bethe formula [12]:

$$\left\langle \frac{dE}{dx} \right\rangle = kz^2 \frac{Z}{A} \frac{1}{\beta^2} \left[ \frac{1}{2} \ln \frac{2m_e c^2 \beta^2 \gamma^2 T_{\text{max}}}{I^2} - \beta^2 - \frac{\delta(\beta\gamma)}{2} \right].$$

It is valid, where the main energy loss originates from ionization effects, i.e. in a region between  $0.1 \lesssim \beta\gamma \lesssim 1000$ . It is a function of the atomic number ( $Z$ ) and the atomic mass of the absorber ( $A$ ). The mean excitation energy ( $I$ ) for silicon is 173 eV [13].  $T_{\text{max}}$  stands for the maximum energy transfer in a single collision. The relevant particle's properties are the velocity ( $\beta$ ), the lorentz factor ( $\gamma$ ) and the charge ( $z$ ) of the incident particle. The density correction  $\delta(\beta\gamma)$  reduces the mean energy loss at high energies because of polarization effects of the material.

Even if widely used, the mean energy loss is a quantity which is “ill-defined experimen-



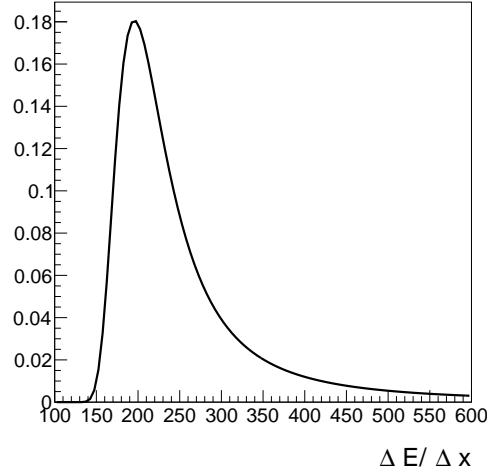


Figure 1.9: Illustration of the shape of a Landau function. Parameters were arbitrarily chosen for this figure.

tally and is not useful for describing energy loss by single particles” [14]. The problem is caused by the underlying probability distribution of one single  $dE/dx$  measurement (this will be named by  $\Delta E/\Delta x$  throughout the following sections), which can be parametrized by a Landau distribution [15]

$$p(x) = \frac{1}{\pi} \int_0^\infty e^{-t \log t - xt} \sin(\pi t) dt.$$

The Landau distribution is a highly asymmetric distribution with a long tail towards the right end (see Fig. 1.9). Theoretically it extends to infinite energies, however in nature the maximal deposited energy is of course limited by the particle’s full energy. The mean and the variance of a landau distribution are not defined. Because of its high assymetry, measurements of  $\langle dE/dx \rangle$  with only a few single measurements are easily biased towards high values, making the mean energy loss described by the Bethe formula to a problematic and unstable concept.

A much better observable is the most probably value (MPV): the maximum of the Landau function. The MPV is much more stable compared to the mean and is not as easily biased towards higher  $dE/dx$  values. The most probable energy loss of a charged particle is defined by the Landau-Vavilov-Bichsel equation [16]:

$$\Delta_p = \xi \left[ \ln \frac{2mc^2 \beta^2 \gamma^2}{I} + \ln \frac{\xi}{I} + j - \beta^2 - \delta(\beta\gamma) \right], \quad (1.1)$$

with  $\xi = (K/Z)\langle Z/A \rangle (x/\beta^2)$ . The thickness of the absorber  $x$  appears explicitly in the Landau-Vavilov-Bichsel equation making the most probable energy loss per path length  $\Delta_p/dx$  logarithmically dependent on  $x$ . A comparison between the Bethe mean energy loss  $\langle dE/dx \rangle$  and the most probable energy loss  $\Delta_p/dx$  is shown in Fig. 1.10. However, when measuring tracks with around  $\sim 15$  hits, it is obviously not too simple to

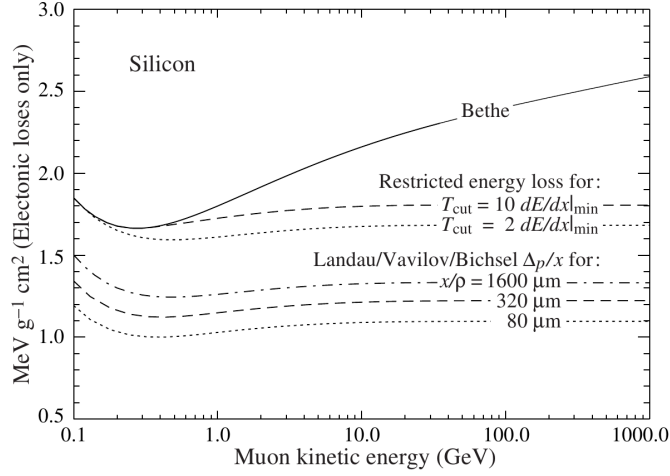


Figure 1.10: Comparison between the Bethe mean energy loss with and without restricted energy loss and the most probable energy loss described by the Landau-Vavilov-Bichsel function for different sizes of thickness. Taken from [14].

extract the most probable value. Large fluctuations can still lead to biases towards higher value of the most probable  $dE/dx$ .

There are several "estimators", which try to suppress as much as possible a bias towards the high end, without introducing a bias to lower values. One of the estimator, also used in the next chapter, is the harmonic-2 estimator

$$I_{h2} = \left( \frac{1}{N} \sum_{i=1}^N (\Delta E / \Delta x)_i^2 \right)^{-1/2}, \quad (1.2)$$

where  $\Delta E / \Delta x$  correspond to one measurement in one tracker module. The harmonic mean of all  $N$  measurements with the power of 2 is then the estimated most probable  $dE/dx$ .

SM particles as pions and muons are minimal ionising in silicon for  $\beta\gamma \sim 4$  (see Fig. 1.11). For higher momenta the deposited energies increase again reaching a plateau at around  $\beta\gamma \sim 100$ . However, new heavy charged particles would mainly be unrelativistic because of their high mass and would therefore deposit much higher energies in the detector. This makes  $dE/dx$  a very well discriminating variable. Thus, the energy loss per path length can be used to discriminate between SM particles and new heavy charged particles, which are usually unrelativistic because of their high mass.

### 1.3.2 Gain calibration of the silicon pixel tracker

During Run I in 2012, the pixel silicon detector was continuously subjected to an energy calibration, a so-called gain calibration. Every pixel was calibrated to the same response, such that the whole pixel tracker should have been well inter-calibrated. Unfortunately, due to various reasons, such as the imperfect constancy of the reference signal, or radiation and temperature induced changes, the energy calibration could not ensure a fully calibrated

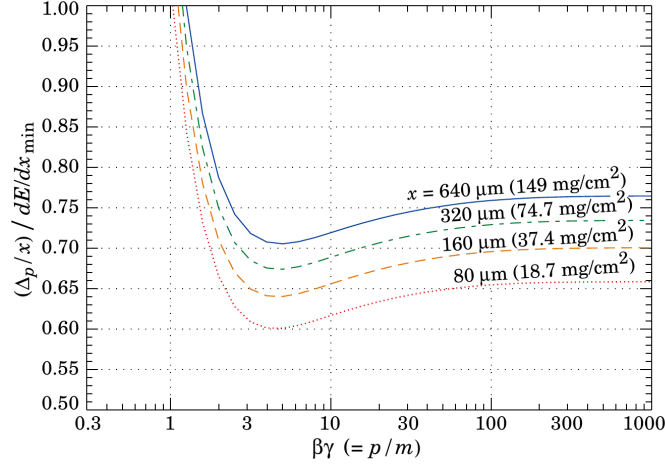


Figure 1.11: Most probable energy loss in silicon, scaled to the mean loss of a minimal ionizing particle ( $388 \text{ eV}/\mu\text{m}$ ). Taken from [14].

pixel tracker. This imperfection of the gain calibration can be seen in Fig. 1.12, where the sum of the harmonic-2 estimator for all tracks  $\sum_{\text{all trks}} I_{h2}$  over the full data-taking period in 2012 is shown. Four different steps can be spotted. The first and the third steps correspond to changes in the settings of the tracker due to irradiation. The second and fourth step show the moment where an online gain calibration was again applied. Unfortunately, although a gain calibration was carried out (even with some delay), it could not bring the average  $dE/dx$  to the same level before the changes in the settings occurred. The size of the difference in the  $dE/dx$  measurement over time being around 15% is too large to use  $dE/dx$  without a further calibration.

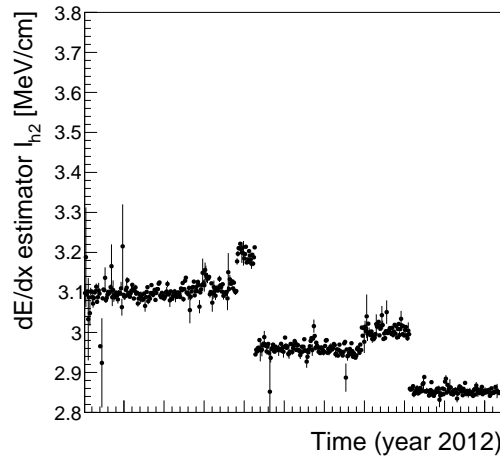


Figure 1.12: Sum of all track's  $dE/dx$  (harmonic-2 estimator) over the full year 2012. Only pixel hits are taken into account. Every data point corresponds to one run.

In the following sections the method of the gain calibration (splitted into an section about the inter-calibration of gain and the absolute calibration of gain) of the pixel silicon tracker is explained. Detailed technical information about the pixel tracker can be found in Sec. ??.

### Inter-calibration of gain

The main goal of the gain calibration is to get a uniform response in the ionization energy loss  $dE/dx$  over the full data taking period in 2012. To ensure also a uniform response of all modules within one time step, also an inter-calibration on module level was carried out. The inter-calibration can in principle be done on various stages: the highest granularity would be a calibration on pixel level, followed by a calibration on ROC-level and then on module-level. Lower granularities in descending order are rings (modules with same z-position) and finally layers (3 layers in the barrel and 4 disks in the endcap). It was checked that all pixels and all ROCs (on one module) are well inter-calibrated, such that the inter-calibration was finally done module-wise. The applied method for the gain calibration of the pixel tracker follows closely the method in [17].

The gain calibration of the pixel silicon tracker has been carried out with the help of minimal ionising particles (MIPs). MIPs in this context are not defined as particles depositing a minimum amount of energy, but more generally a small amount of energy. This denotes all particles located at the plateau of the  $dE/dx$  distribution vs. momentum (see Fig. 1.11). It ensures that all particles deposit a rather similar amount of energy such that the variation due to different momenta is suppressed. The small ionisation for particles was ensured with a momentum selection of  $p > 2$  GeV. Additionally, only tracks with at least eight hits and a  $\chi^2/n.d.o.f. < 3$  to ensure a good reconstruction were used. For the calibration a sample containing around 50 million “minimum bias” events is used which is specifically recorded for tracker calibration purposes. “Minimum bias” means that neither an online nor offline selection was applied.

For every module in the pixel tracker (there are 1440 modules in total), a distribution of the energy loss per path length  $\Delta E/\Delta x$  is built. Fig. 1.13 shows an example distribution for one module. The underlying Landau distribution can be nicely seen. To extract the MPV for every module a fit to the core distribution is performed. The fit is done with a Landau convoluted with a Gaussian function to be closer to the experimentally observed energy spectrum. This also increases the fit performance and the stability of the fit. The measurement of  $\Delta E/\Delta x$  is done in ADC counts per mm. ADC counts are a measure for the deposited charge after digitization. It consists out of a unsigned 16-bit integer (ranging from 0 to 65 535). The path length  $\Delta x$  is calculated with

$$\Delta x = d_{\text{module}_i} \cdot \cos(\phi_{\text{track}}),$$

where  $d_{\text{module}_i}$  is the thickness of module  $i$  and  $\phi_{\text{track}}$  is the relative angle of the particle’s trajectory to the axis normal of the module. With the measured MPV extracted from the fit, an inter-calibration factor is calculated for every module

$$c_{\text{inter}} = \frac{\text{MPV} [\text{ADC/mm}]}{\text{MPV}_{\text{target}} [\text{ADC/mm}]} = \frac{\text{MPV} [\text{ADC/mm}]}{300 \cdot 265 \text{ ADC/mm}}.$$

The factor  $300 \cdot 265 \text{ ADC/mm}$  is in principal an arbitrary number. However, it was chosen

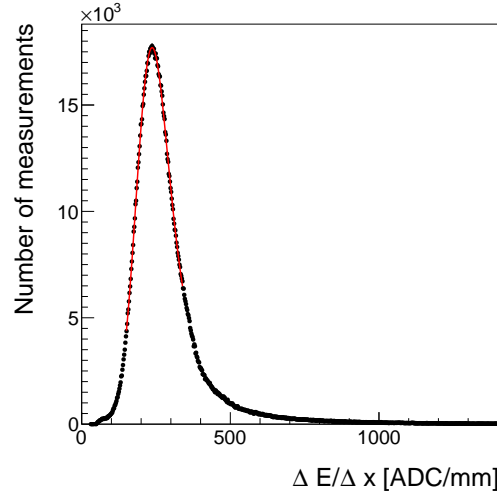


Figure 1.13: An example of the  $\Delta E/\Delta x$  distribution measured in ADC count per mm for one module of the CMS pixel tracker. A Landau convoluted with a Gaussian is fitted to the core of the distribution in an iterative procedure.

such that it corresponds approximately to the most probably energy deposition of a MIP. The calibration factor can then be used to scale every single measurement in a module to a calibrated  $\Delta E/\Delta x$  measurement

$$\frac{\Delta E}{\Delta x_{\text{calibrated}}} = \frac{\Delta E_{\text{uncalibrated}}}{c_{\text{inter}}}$$

The determination of the calibration factor needs to be done for every of the five time steps, shown in Fig. 1.12 independently, in order to get rid of the time dependency. The result of the inter-calibration can be seen in Fig. 1.14. The variation over time was indeed eradicated, resulting in a maximal time variation of less than  $\sim 1\%$ .

Additionally, the same procedure is carried out for a corresponding simulated data sample to ensure also the inter-calibration of the pixel modules on all simulated samples.

### Absolute calibration of gain

As a final step, the targeted MPV being  $\text{MPV}_{\text{target}} = 300 \cdot 265 \text{ ADC/mm}$  needs to be translated to a meaningful physical quantity given in physical units (e.g. MeV/cm). That means, that the charge measurement in ADC counts needs to be converted to the real energy release of a particle. The relation between  $\Delta E$  in ADC counts and the energy loss in eV is given by

$$\Delta E [\text{eV}] = \frac{\Delta E [\text{ADC}]}{c_{\text{inter}}} \cdot \frac{N_e}{\text{ADC}} \cdot 3.61 \text{ eV},$$

where  $N_e/\text{ADC}$  is the number of electrons which correspond to one ADC count and 3.61 eV is the mean energy needed to create one electron-hole pair in silicon at  $-10^\circ\text{C}$ . Such an absolute gain calibration can be done with the help of several methods (all explained in [17]). For the absolute calibration of the silicon pixel tracker, it can be taken advantage

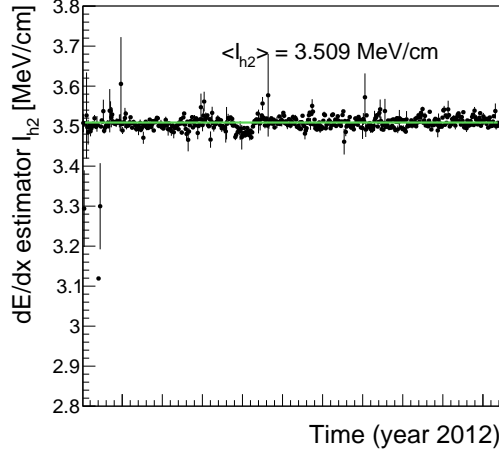


Figure 1.14: Sum of all track's  $dE/dx$  (harmonic-2 estimator) over the full year 2012 after applying the calibration factors, resulting in an average  $dE/dx$  of 3.51 MeV/cm. Only pixel hits are taken into account. Every data point corresponds to one run.

of the already conducted absolute calibration of the silicon strip detector. In [17], the absolute gain calibration was done with the help of the most probable energy release per path length of muons, theoretically described by the Landau-Vavilov-Bichsel formula in Eq. 1.1. To calibrate the pixel tracker to the correct energy loss per path length it is therefore sufficient to determine one calibration factor to relate the average  $dE/dx$  of all tracks in the pixel tracker as shown in Fig. 1.14 to the average measured  $dE/dx$  in the strip tracker, shown in Fig. 1.15 by

$$c_{\text{absolute}} = \frac{dE/dx_{\text{strip}}}{dE/dx_{\text{pixel}}} = \frac{3.303}{3.509} = 0.941.$$

This factor is then applied on top of  $c_{\text{inter}}$  for all pixel modules.

Finally, also for the simulated samples an absolute calibration factor needs to be determined, where the simulated pixel tracker is calibrated to the average  $dE/dx$  of the silicon strip measured in data.

### 1.3.3 Asymmetric Smirnov discriminator

As mentioned before, a difficult task when measuring the energy deposition of a particle consists in finding a robust estimator for the MPV of the underlying Landau, i.e combining eventually only a few single measurements of  $\Delta E/\Delta x$  to one single  $dE/dx$  estimator. The harmonic-2 estimator  $I_{h2}$  was already introduced in Sec. 1.3.1 in Eq. 1.2. It is known as a robust estimator not easily biased by large fluctuation in  $\Delta E/\Delta x$  because of the suppression by a factor of 2.

However, it was shown in [17] that a better discrimination between SM particles and possible new heavy particles can be achieved when using likelihood techniques, i.e. de-

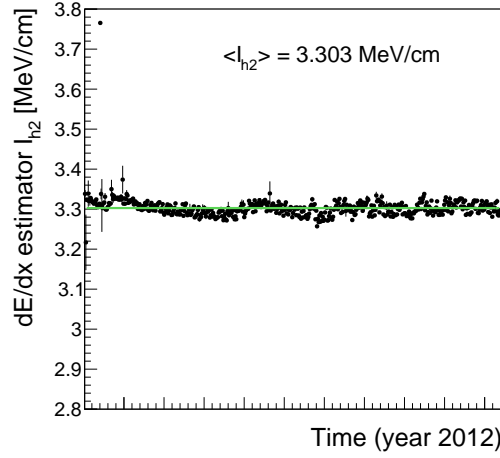


Figure 1.15: Sum of all track's  $dE/dx$  (harmonic-2 estimator) measured in the silicon strip detector over the full year 2012. The average most probable  $dE/dx$  is  $I_{h2} = 3.303$  MeV/cm. Every data point corresponds to one run.

termining the probability that the set of all  $\Delta E/\Delta x$  belonging to one track is actually compatible with the hypothetical probability distribution of a MIP.

Testing that a measured sample has been drawn from a specific distribution is known as the Smirnov-Cramér-von Mises test [18,19], which is deduced from the integral of the squared difference of the measured distribution  $P_N(x)$  to the hypothesis distribution  $P(x)$

$$I_s = \int_{-\infty}^{\infty} [P_N(x) - P(x)]^2 dP(x)$$

leading to a test statistics of

$$I_s = \frac{3}{N} \cdot \left( \frac{1}{12N} + \sum_{i=1}^N \left[ P_i - \frac{2i-1}{2N} \right]^2 \right),$$

where  $P_i$  is the cumulative probability that a MIP would release a  $\Delta E/\Delta x$  equal or smaller than the measured  $\Delta E/\Delta x$  with all  $P_i$  are arranged in increasing order.

However, this test statistics is not sensitive to whether there are incompatibilities because of higher or lower variations compared to the hypothesis distribution. It is therefore not really suitable for the discrimination between MIPs and heavy new particles by  $dE/dx$ . A so-called Asymmetric Smirnov-Cramér-von Mises discriminator was developed in [17] which is only sensitive to incompatibilities to the MIP hypothesis towards higher energy depositions

$$I_{as} = \frac{3}{N} \cdot \left( \frac{1}{12N} + \sum_{i=1}^N \left[ P_i \cdot \left( P_i - \frac{2i-1}{2N} \right)^2 \right] \right).$$

A value of  $I_{as}$  close to zero indicates good compatibility with the MIP hypothesis, whereas

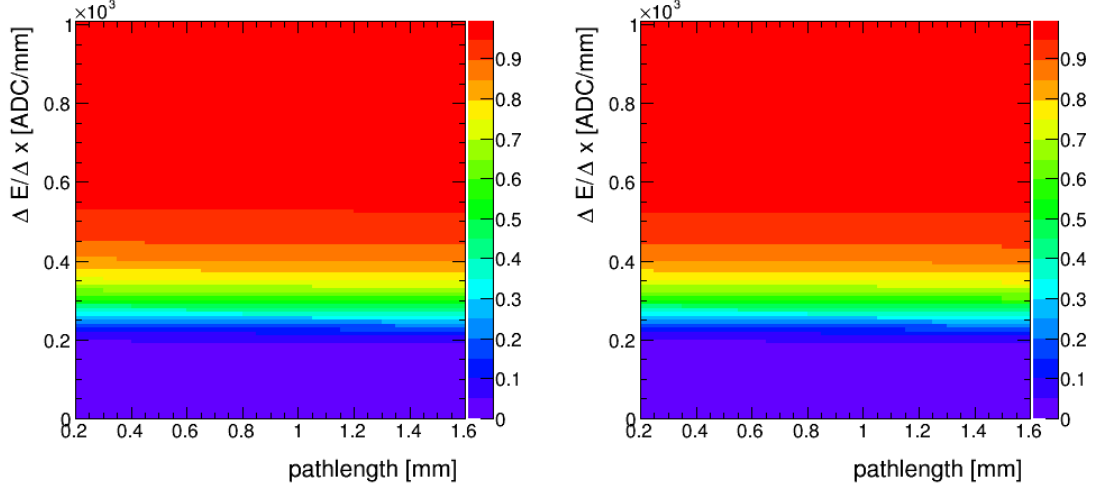


Figure 1.16: Cumulative probability for a MIP to release a  $\Delta E/\Delta x$  (y-axis) vs. the pathlength (x-axis) in data (left) and simulation (right) for the pixel tracker.

a value close to one indicates worse compatibility because of too large energy loss.

The underlying probability distribution of the energy release for a given path length in the pixel tracker is extracted from the same “Minimum bias” sample used for the pixel energy calibration. In total 28 different templates each for a different given path length are created. The corresponding templates for the energy release in the silicon strip detector were already built by [17]. In Fig. 1.16 the probability distribution template for the pixel tracker in data and simulation is shown. A comparison between data and simulation of  $I_{\text{as}}$  and  $I_{\text{h2}}$  for high-purity tracks (as defined in [?]) with  $p_{\text{T}} > 10 \text{ GeV}$  and  $|\eta| < 2.1$  can be found in Fig. 1.17. It shows discrepancies up to 100% which is caused by the non-optimal simulation of  $dE/dx$ .

As already pointed out several times, the goal of including the pixel energy information is to increase the discrimination power of  $I_{\text{as}}$  between background and signal, especially for short tracks. In Fig. 1.18 (left plot), a comparison of the shapes of background tracks and signal tracks in simulated samples without any selection is shown (details about simulated samples can be found in Sec. 1.4). It can be seen, that the  $I_{\text{as}}$  distribution of the signal tracks shows a much longer tails toward the right end of the plot, whereas the background is rather distributed close to zero. Not only the mass of the signal track influences the  $I_{\text{as}}$  distribution but also the number of hits of a signal track which in turn define the influence of fluctuations of single  $\Delta E/\Delta x$  measurements on the  $I_{\text{as}}$  discriminator. This is also shown in Fig. 1.18 (right plot).

### 1.3.4 Efficiency improvements

In order to quantify the impact of the additional pixel  $\Delta E/\Delta x$  information on an analysis selection, the signal selection efficiency over the background selection efficiency for different selection cuts of  $I_{\text{as}}$  is drawn in Fig. ???. As can be seen, the improved background suppression for a given signal selection efficiency depends on the mass and on the lifetime



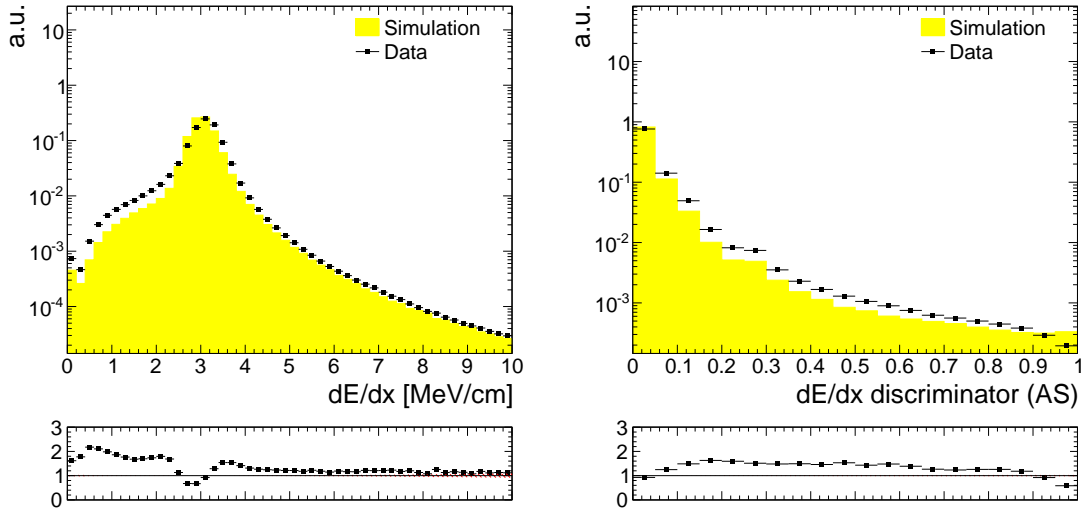


Figure 1.17: Normalized  $I_{as}$  and  $I_{h2}$  distributions in data and simulation for high-purity tracks (as defined in [?]) with  $p_T > 10$  GeV and  $|\eta| < 2.1$ .

of the chargino. For masses of blablab, improvements in the background suppression of .... can be achieved. For low lifetimes, the additionnaly improves up to a factor of ....

- Show comparison of  $I_{as}$  comparing pixel and strip
- Show plot with  $I_{as}$  distribution for bkg and signal (give reference to next chapter)
- not a long section

In Fig. ??, a comparison between signal sample and background dedx is shown. It can be already seen that  $I_{as}$  is well discriminating.

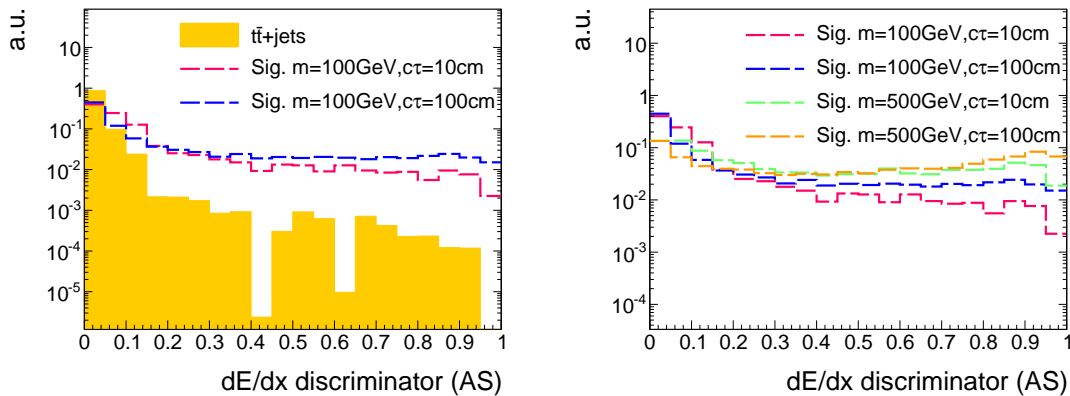


Figure 1.18: Distribution of  $I_{as}$  for background tracks and signal tracks (left plot) and a comparison between four different signal models ( $m=100$  GeV,  $500$  GeV,  $c\tau = 10$  cm,  $100$  cm) (right plot).

## 1.4 Simulated samples

- Event weights applied for correct Pileup modelling
- Detailed information can be found in Experimental setup chapter
- Think what to write in the detector chapter to be not wiederholend

Detector chapter:

- THINK!

### 1.4.1 SM samples

- Title: Background samples
- To study the background, following samples were used: ... generated with ...
- Not all SM processes samples were availbale
- Not so dramatic, because data based bkg estimation method
- Main Background are ... ???
- Only a few were available and thus processed
- Most important sample was included: Wjets
- ZoNuNu Backgorund not availbale plays also a role (see DT paper!)
- Table of SM samples with cross-sections

### 1.4.2 Signal samples

- Lifetime reweighting
- Simulation of lifetime in Geant
- Trigger emulation
- What samples are exactly generated.
- Madgraph+Pythia
- Chargino Pair production + Chargino neutralino production
- Table with generated signal samples with cross-sections???? No

## 1.5 Event selection

### 1.5.1 Datasets and triggers

- Datasets and triggers used in the analysis
- signal samples generated with Madgraph and pythia
- They are decayed in Geant to only pions. Around ten different lifetimes were simulated
- For other lifetimes: lifetime reweighting is done PLOT
- For five different masses (100-500 GeV)

### 1.5.2 Preselection

- Motivate different selection cuts
- Reference DT search for most of them

### 1.5.3 Main discriminating variables

- $dE/dx$
- $pt$
- Show some MC signal bkg comparison plots (only Wjets?)

## 1.6 Sources of backgrounds

- Background consist of particles which make high energy deposits and are high  $pt$
- In general: Low background search

### 1.6.1 Fake tracks

- Definition of fake tracks
- How can they fake the signal

### 1.6.2 Muons

- How can muons fake the signal

### 1.6.3 Pions

- How can pions fake the signal

### 1.6.4 Electrons

- How can electrons fake the signal

## **1.7 Background estimation methods**

### **1.7.1 Fake background**

### **1.7.2 Leptonic background**

### **1.7.3 Systematic uncertainties**

## **1.8 Optimization of search sensitivity**

- Show plots
- show table
- Include NlostOuter here, too

## **1.9 Statistical Methods/ Limit setting**

## **1.10 Results**

- Data cutflowtable
- Tables with results
- One plot (4 bins: Prediction and data)

## **1.11 Interpretation**

### **1.11.1 Systematic uncertainties of simulated signal samples**

### **1.11.2 Exclusion limits**

- 1-d limits
- 2-d limits

## Bibliography

- [1] CMS Collaboration, “Search for new physics in the multijet and missing transverse momentum final state in proton-proton collisions at  $\sqrt{s}=8$  TeV”, *JHEP* **06** (2014) 055, [arXiv:1402.4770](#). doi:10.1007/JHEP06(2014)055.
- [2] CMS Collaboration, “Searches for Supersymmetry using the  $M_{T2}$  Variable in Hadronic Events Produced in pp Collisions at 8 TeV”, *JHEP* **05** (2015) 078, [arXiv:1502.04358](#). doi:10.1007/JHEP05(2015)078.
- [3] ATLAS Collaboration, “Search for squarks and gluinos with the ATLAS detector in final states with jets and missing transverse momentum using  $\sqrt{s}=8$  TeV proton-proton collision data”, *JHEP* **09** (2014) 176, [arXiv:1405.7875](#). doi:10.1007/JHEP09(2014)176.
- [4] M. Ibe, S. Matsumoto, S. Shirai et al., “Wino Dark Matter in light of the AMS-02 2015 Data”, *Phys. Rev.* **D91** (2015), no. 11, 111701, [arXiv:1504.05554](#). doi:10.1103/PhysRevD.91.111701.
- [5] T. Moroi, M. Nagai, and M. Takimoto, “Non-Thermal Production of Wino Dark Matter via the Decay of Long-Lived Particles”, *JHEP* **07** (2013) 066, [arXiv:1303.0948](#). doi:10.1007/JHEP07(2013)066.
- [6] J. Hisano, S. Matsumoto, and M. M. Nojiri, “Explosive dark matter annihilation”, *Phys. Rev. Lett.* **92** (2004) 031303, [arXiv:hep-ph/0307216](#). doi:10.1103/PhysRevLett.92.031303.
- [7] CMS Collaboration, “Searches for long-lived charged particles in pp collisions at  $\sqrt{s}=7$  and 8 TeV”, *JHEP* **07** (2013) 122, [arXiv:1305.0491](#). doi:10.1007/JHEP07(2013)122.
- [8] CMS Collaboration, “Search for disappearing tracks in proton-proton collisions at  $\sqrt{s}=8$  TeV”, *JHEP* **01** (2015) 096, [arXiv:1411.6006](#). doi:10.1007/JHEP01(2015)096.
- [9] CMS Collaboration, “Reinterpreting the results of the search for long-lived charged particles in the pMSSM and other BSM scenarios”, *CMS Physics Analysis Summary* **CMS-PAS-EXO-13-006** (2014).
- [10] CMS Collaboration, “Phenomenological MSSM interpretation of the CMS 2011 5fb-1 results”, *CMS Physics Analysis Summary* **CMS-PAS-SUS-12-030** (2013).
- [11] CMS Collaboration, “Description and performance of track and primary-vertex reconstruction with the CMS tracker”, *JINST* **9** (2014), no. 10, P10009, [arXiv:1405.6569](#). doi:10.1088/1748-0221/9/10/P10009.

- [12] H. Bethe, “Theory of the Passage of Fast Corpuscular Rays Through Matter”, *Annalen Phys.* **5** (1930) 325–400. [Annalen Phys.397,325(1930)].  
doi:10.1002/andp.19303970303.
- [13] “National Institute of Standards and Technology”.  
<http://physics.nist.gov/cgi-bin/Star/compos.pl?mode=text&matno=014>.  
Accessed: 2015-10-21.
- [14] Particle Data Group Collaboration, “Review of Particle Physics”, *Chin. Phys.* **C38** (2014) 090001. doi:10.1088/1674-1137/38/9/090001.
- [15] L. Landau, “On the energy loss of fast particles by ionization”, *J. Phys.(USSR)* **8** (1944) 201–205.
- [16] H. Bichsel, “Straggling in Thin Silicon Detectors”, *Rev. Mod. Phys.* **60** (1988) 663–699. doi:10.1103/RevModPhys.60.663.
- [17] L. Quertenmont, “Search for Heavy Stable Charged Particles with the CMS detector at the LHC”. PhD thesis, Louvain, U., 2010.
- [18] T. W. Anderson, “On the Distribution of the Two-Sample Cramr-von Mises Criterion”, *The Annals of Mathematical Statistics* **33** (1962), no. 3, pp. 1148–1159.
- [19] F. James, “Statistical methods in experimental physics”. 2006.

